Effect of BaTiO₃ powder as an additive in perovskite films on solar cells

Chuanxiang Zhang, [ID] [a] Xiqiang Li,[b] Lingling Ding,[b] Chen Jin[a] and Haijun Tao*[b]

Perovskite solar cells (PSCs) are considered to be ideal energy devices, where perovskite-type organic metal halides act as light-absorbing materials. In PSCs, the photoexcitons are extracted and separated to afford high photoelectric conversion efficiency under the action of the built-in electric field (E_{bi}). However, the current challenge is that a low E_{bi} cannot provide a sufficient driving force to separate photonic excitons, which causes the captured charges to escape from the deep energy-level defect state. Here, the ferroelectric material barium titanate (BaTiO₃) was directly introduced into the perovskite precursor solution to reduce the defection density (to 8.58×10^{17} cm^{-3}) in PSCs and promote the separation of photoexcitons. Furthermore, the addition of BaTiO₃ improved the quality of the perovskite film and significantly increased the photoelectric performance after the polarization treatment. This is mainly attributed to the residual polarization electric field generated by ferroelectric polarization, which increased the E_{bi} of the PSCs and the width of the depletion layer and inhibited the non-radiative recombination of carriers. This work provides a possibility to design and develop optoelectronic devices with high-efficiency optoelectronic response behavior.

1 Introduction

Organic–inorganic hybrid perovskite (OIHP) materials have become a bright-star material because of their excellent optical and electrical properties and simple and low-cost synthetic methods. Since the first report from Miyasaka's research group in 2009, the photoelectric conversion efficiency (PCE) of PSCs has rapidly increased from an initial 3.8% (ref. 1) to a certified 25.5% (ref. 2) in just ten years. Despite this rapid development, the PCE of PSCs is still far below the S–Q limitation (33.5%) of single-junction solar cells due to the non-radiative recombination of carriers in PSCs. The main causes of carrier recombination are poor quality of the perovskite film, material interface mismatch, and low built-in electric field. At present, the first two factors are mainly investigated and analyzed in view of perovskite crystallization engineering, defect passivation engineering, and interface engineering,[3–6] whereas studies on improving cell performance based on increasing E_{bi} are still few. Therefore, when other optimization methods cannot further improve the overall performance of PSCs, we consider that carrier separation and transmission can be regulated by enhancing the E_{bi} with the aim of reducing the occurrence of non-radiative recombination.

The first method to increase the E_{bi} of the cell is to apply an external electric field on the photoactive layer of photovoltaic devices to suppress carrier recombination at the capture site. Chen *et al.*[7] first proved the ferroelectric property of MAPbI₃ through the phase change of the piezoelectric microscope (PFM), and further verified that pressurized polarization can regulate the interface energy-band structures of PSCs for charge separation under certain circumstances. Zhang *et al.*[8] developed an external electric field-assisted annealing treatment technology, which can control the ion polarization direction of perovskite films. Therefore, a good perovskite crystal film obviously enhances the internal electric field and effectively promotes charge separation and transport, leading to an increase in the PCE of PSCs from 16.77% to 19.18%. This method of carrier transport assisted by an external electric field mainly relies on the recognition of the ferroelectric properties of OIHP materials. Although researchers have confirmed this conclusion by theoretical calculation,[9–11] PFM observation,[7] and hysteresis loop measurement (P–E),[12,13] Fan *et al.*[14] did not observe the existence of ferroelectric domains in MAPbI₃, and the P–E test results also showed that MAPbI₃ did not have ferroelectric properties. Therefore, whether this material has ferroelectricity is still controversial. Since it is impossible to determine whether the ferroelectricity of MAPbI₃ exists or not, we should focus on the utilization of the electric field to promote carrier separation. However, it is not difficult to understand that this is not a persistent and stable method because the applied electric field is easily shielded by ion migration or accumulated charges. On this basis, we hope to develop a material that can maintain

School of Materials Science and Engineering, Nanjing Institute of Technology, Nanjing 211167, China

College of Materials Science and Technology, Nanjing University of Aeronautics and Astronautics, Nanjing 211106, China. E-mail: taohaijun@nuaa.edu.cn

permanent polarization and provide a stable and controllable electric field for optoelectronic devices.

Based on the knowledge of ferroelectric materials, we think about their residual polarization field. Ferroelectric materials are introduced into the PSCs to change the remaining polarization electric field through the external electric field, finally regulating the ion and carrier transports. This idea was firstly used in the fields of photovoltaic organic solar cells (OPV) and dye sensitized solar cells (DSSC). Researchers introduced inorganic ferroelectric materials ($SrTiO_3$, $BaTiO_3$, *etc.*) and organic ferroelectric materials [PVDF, P(VDF-TrFE), *etc.*] into OPV light absorption layer, anionic buffer layer, and photoanode of DSSC, respectively, causing better photoelectric performance.[15–18] PSCs are developed from DSSC with similar principles. In view of the successful application of ferroelectric materials in DSSC, researchers are aiming at introducing ferroelectric materials into PSCs to further improve their efficiency.[19–24] At present, the introduction of ferroelectric materials has three locations or functions: replacing TiO_2 as ETL, inserting at the ETL/perovskite layer or the perovskite/HTL interface, and forming the perovskite layer. The former two methods are common, and the latter method is only used for organic materials P(VDF-TrFE).

In this work, in order to improve the E_{bi} of PSCs, we selected the inorganic ferroelectric material, $BaTiO_3$, which induced strong spontaneous polarization and had the same structure as that of the perovskite film to prepare the composite optical absorption layer. Subsequently, the corresponding microstructures and chemical compositions were characterized in detail to support the mechanistic analyses on the carrier transport. Also, the photoelectric performance of the PSCs with the introduction of ferroelectric materials was measured around the two aspects of photoelectric conversion efficiency and interfacial state. This work will provide a possibility to design and develop optoelectronic devices with high-efficiency optoelectronic response behavior.

2 Experimental

2.1 Materials

Isopropyl titanate (99%), titanium tetrachloride (99%), chlorobenzene (99.5%), isopropanol (99.8%), barium titanate (<100 nm, 99.9%), and graphite (8000 mesh, 99.95%) were all purchased from Aladdin Reagent (Shanghai) Co., Ltd. Lead iodide (99%), dimethyl sulfoxide (DMSO, 99%), and *N,N*-dimethylformamide (DMF, 99.9%) were all purchased from Sigma-Aldrich. Ethyl cellulose (CP, M70) was provided by Sinopharm Chemical Reagents Co. Ltd. Carbon black (30–45 nm) was purchased from Nanjing Xianfeng Nano Co., Ltd; TiO_2 slurry (NJV-30NR-D) and ammonium methyl iodide (99%) were provided by Sunlight New Energy Co., Ltd and Maitidevi Chemical New Material Technology Co., Ltd, respectively. The FTO conductive glasses with the resistance of 7–8 Ω □$^{-1}$ were provided by Shandong Opivite New Energy Technology Co., Ltd.

2.2 $BaTiO_3$@MAPbI$_3$ precursor solution preparation

Firstly, 3000 μL mixed solution of DMF and DMSO (volume ratio of 4 : 1) was prepared and placed in bottle A for later use. 40 mg

$BaTiO_3$ powders were accurately weighed and placed into bottle B, where the above mixed solution (1000 μL) in bottle A was added. Then, the ultrasonic treatment was carried out until the powders were evenly dispersed into the solution. Subsequently, 1500 μL mixed solution of DMF and DMSO was sucked into bottle C, where 2.4 M MAI and PbI_2 were added.

For 0.5 wt% $BaTiO_3$@MAPbI$_3$ precursor solution, we took 300 μL of the solution in bottle A, 100 μL of the solution of bottle B, and 400 μL of the solution of bottle C to form the precursor solution. Also, the mixed solution including 200 μL bottle A solution, 200 μL bottle B solution, and 400 μL bottle C solution could form 1.0 wt% $BaTiO_3$@MAPbI$_3$ precursor solution. The 2.0 wt% $BaTiO_3$@MAPbI$_3$ precursor solution included 400 μL solution of bottle B and 400 μL solution of bottle C. All these precursor solutions would be stirred at 60 °C for use in device fabrication.

2.3 Device fabrication

After cleaning the FTO conductive glasses, we coated their surfaces with the compact layer solution at 2000 rpm for 60 s, which was followed by heat treatment at 500 °C for 30 min. The TiO_2 precursor was prepared by diluting TiO_2 slurry with alcohol at a mass ratio of 1 : 7, then it was spun onto the surface of the above compact layer at the speed of 3000 rpm for 30 s. Also, the as-prepared TiO_2 precursor was treated at 500 °C for 30 min. The prepared FTO conductive glasses were immersed in $TiCl_4$ solution, soaked at 70 °C for 30 min, and then treated at 500 °C for 30 min. The as-prepared $BaTiO_3$@MAPbI$_3$ precursor was spin-coated onto the surface of the modified layer by a two-step spin-coating method (1000 rpm, 10 s and 5000 rpm, 30 s). 250 μL chlorobenzene was dripped onto the spin-coated film. Afterward, annealing treatment was carried out on the heating platform in two steps (60 °C, 2 min; 120 °C, 10 min). Finally, the carbon slurry (including ethyl cellulose, carbon black, graphite, ethyl cellulose solution, and chlorobenzene) was scraped onto the surface of the perovskite layer and annealed at 100 °C for 1 h to complete the assembly of the whole cell. Also, the whole assembly process of the cell was completed in air. The fabrication process of the $BaTiO_3$@MAPbI$_3$ composite film with a certain content (0.5 wt%, 1.0 wt%, and 2.0 wt%) of $BaTiO_3$ powders in the perovskite precursor solution, as shown in Fig. 1.

2.4 Characterization

X-ray diffraction (XRD, RIGAKU Ultima IV) was used to characterize the crystal structure of the samples. Spectroscopy (Renishaw in Via) was used to characterize the phase structure of $BaTiO_3$ nanoparticles. Field emission scanning electron microscopy (FE-SEM, Zeiss Merlin Compact) was used to characterize the surface and section morphologies. The *J–V* characteristic curves of C-PSCs were obtained using the full spectrum solar simulator (Model 91192, Newport Co.), equipped with a Keithley digital source meter (Keithley 2400), and the effective area was set to 0.15 cm². The EQE characterization of the C-PSCs was carried out by an external quantum test system (Oriel's IQE 200) in the wavelength range of 300–900 nm.
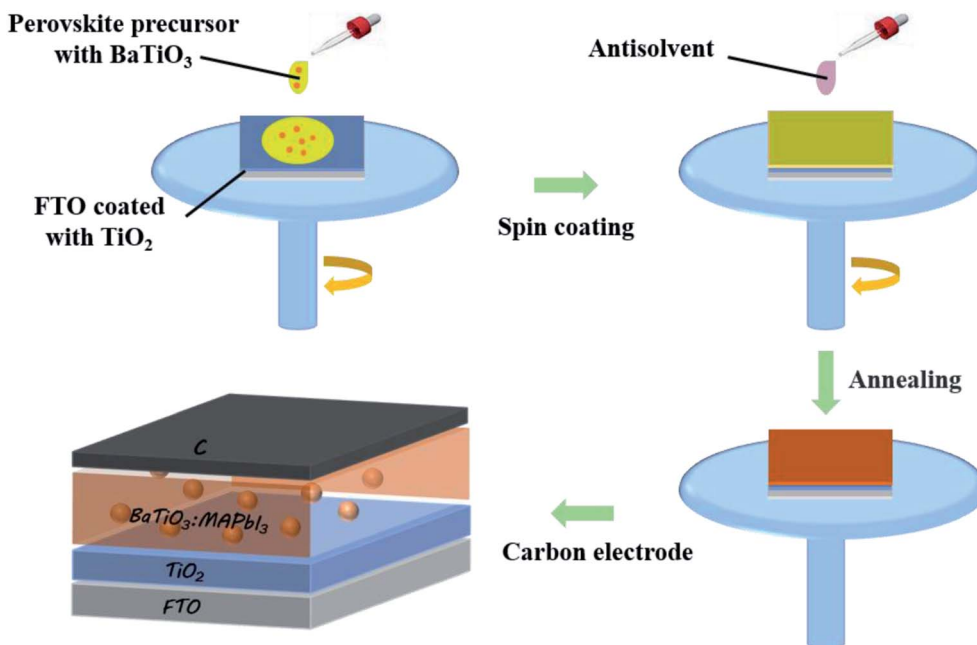
Fig. 1 BaTiO$_3$@MAPbI$_3$ composite film and the device preparation processes.

An electrochemical workstation (Shanghai Chenhua C660E) was used to evaluate the corresponding electrochemical performances. The electrochemical impedance test amplitude was 10 mV with test frequency in the range of 1–1 MHz, and the Mott–Schottky test frequency of 10 kHz. The excitation voltage of the photoluminescence test system (PTI QM40-NI) was 3 V, the light source wavelength in the system was 355 nm, and the test wavelength range was 650–850 nm. All the characterizations were carried out in the atmosphere without any encapsulation.

3 Results and discussion

From the point-view of the structural features, ferroelectricity is an electron/ion polarization phenomenon in the typical perovskite BaTiO$_3$ materials, which is caused by the displacement of the Ti^{4+} cation in the TiO$_6$ octahedron from the center. This process results in a decrease in the symmetry between the unit cell and the cubic lattice, and the structural transformation from the cubic phase to the tetragonal phase. Also, the phase structure directly determines the ferroelectricity of BaTiO$_3$; therefore, it needed to analyze the crystal structures of BaTiO$_3$ materials.

Tetragonal BaTiO$_3$ (T-BaTiO$_3$) nanoparticles were prepared by the simple sintering treatment on cubic BaTiO$_3$ (C-BaTiO$_3$) nanoparticles at 800 °C.[25] Firstly, the crystal structures of the two BaTiO$_3$ were verified by XRD, as shown in Fig. 2(a). C-BaTiO$_3$ shows a single peak at $2\theta = 45°$ corresponding to the (200) crystal plane, which is consistent with the cubic BaTiO$_3$ structure of the $Pm\bar{3}m$ space group (JCPDS no. 79-2263). On the other hand, the splitting phenomenon of the peak of T-BaTiO$_3$ is also observed at the position of about $2\theta = 45°$ (upper right inset), where 44.8° and 45.2° correspond to the (002) and (200) crystal planes of BaTiO$_3$, respectively. It matches well with the

tetragonal BaTiO$_3$ structure (JCPDS no. 05-0626). Raman spectroscopy is an advantageous technique to analyze the cubic-tetragonal symmetry of BaTiO$_3$ nanoparticles. Fig. 2(b) shows the Raman spectrum of the BaTiO$_3$ powders after sintering. Among them, the two Raman peaks at 305 cm^{-1} and 717 cm^{-1} are the characteristic peaks of tetragonal BaTiO$_3$, indicating that T-BaTiO$_3$ has a tetragonal crystal structure at room temperature.[26]

As shown in Fig. 3(a and b), it can be obviously seen that there are many pinholes on the surface of the film without the addition of BaTiO$_3$, and many white spots are distributed at the grain boundaries. According to the literature reports, it can be determined that these white spots are residual PbI$_2$.[27] After adding BaTiO$_3$, the pinholes on the surface of the MAPbI$_3$ film disappeared, the surface was uniform and dense, and the number of small white particles also decreased to a certain extent. The average grain size of MAPbI$_3$ increased from 0.47 μm to 0.51 μm. The main reason was that both BaTiO$_3$ and MAPbI$_3$ had an octahedral structure. A similar structure allows BaTiO$_3$ to be used as the seed layer to induce the crystal growth of the MAPbI$_3$ film, and the crystal grain size increases significantly. Since the grain boundary in the MAPbI$_3$ film can be used as a trap center, it is an important factor to cause the non-radiative recombination of carriers.[28] Therefore, the increase in the crystal grain size can effectively suppress the occurrence of non-radiative recombination and increase the open circuit voltage and filling factor of the device. Fig. 3(c and d) shows the cross-sectional views of the sample before and after the addition of BaTiO$_3$. It can be seen that the thickness of the perovskite layer does not change significantly. When BaTiO$_3$ is not added, there is a large gap between the MAPbI$_3$ film and the substrate, causing the interruption of the carrier transport channel and adversely affect the carrier transport. The addition of BaTiO$_3$
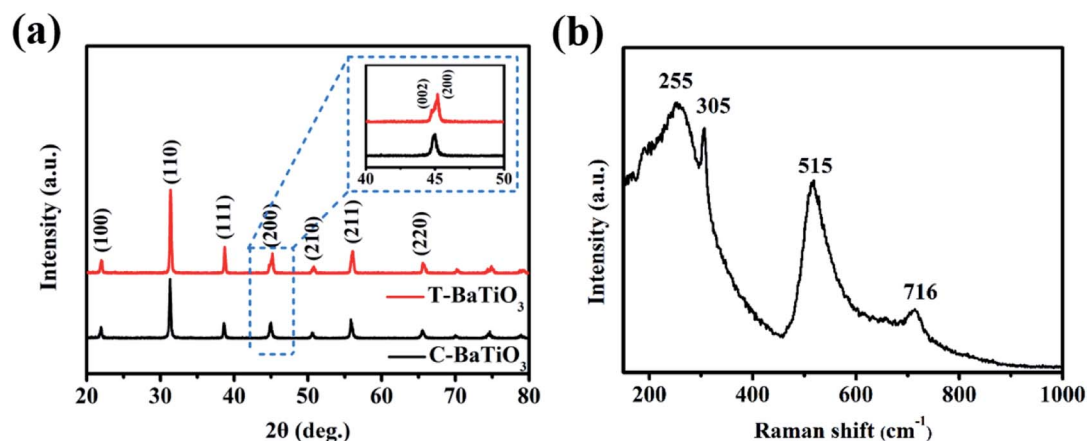
Fig. 2 (a) XRD patterns of BaTiO$_3$ powders before and after sintering. (b) Raman spectrum of BaTiO$_3$ powders after sintering.

completely covers the substrate, which is conducive for the transport of carriers. At the same time, it can be seen that the surface of the MAPbI$_3$ film with BaTiO$_3$ is smoother without obvious protrusions. The relatively smooth surface can also improve the interface contact between the MAPbI$_3$ film and the carbon electrode, promoting the transfer of holes, and effectively inhibiting carrier recombination. However, it is not the main factor affecting the inhibition of carrier recombination, compared with the addition of BaTiO$_3$.

In order to investigate the influence of the BaTiO$_3$ doping amount on the crystallization properties of the MAPbI$_3$ film, the

XRD diffraction pattern was used to characterize the film, as shown in Fig. 4(a). The film has two strong diffraction peaks at 14.11° and 28.45°, corresponding to the MAPbI$_3$ (110) and (202) crystal planes. The results show that no new diffraction peaks appear at the XRD diffraction pattern after doping the BaTiO$_3$ nanoparticles. This indicates that the addition of BaTiO$_3$ does not change the tetragonal crystal structure of MAPbI$_3$. However, after normalizing the (110) diffraction peak, it is found that the FWHM decreases from 0.228° to 0.173° after adding BaTiO$_3$. The addition of BaTiO$_3$ nanoparticles can increase the crystallinity of the MAPbI$_3$ film. According to the Scherrer formula $D =$
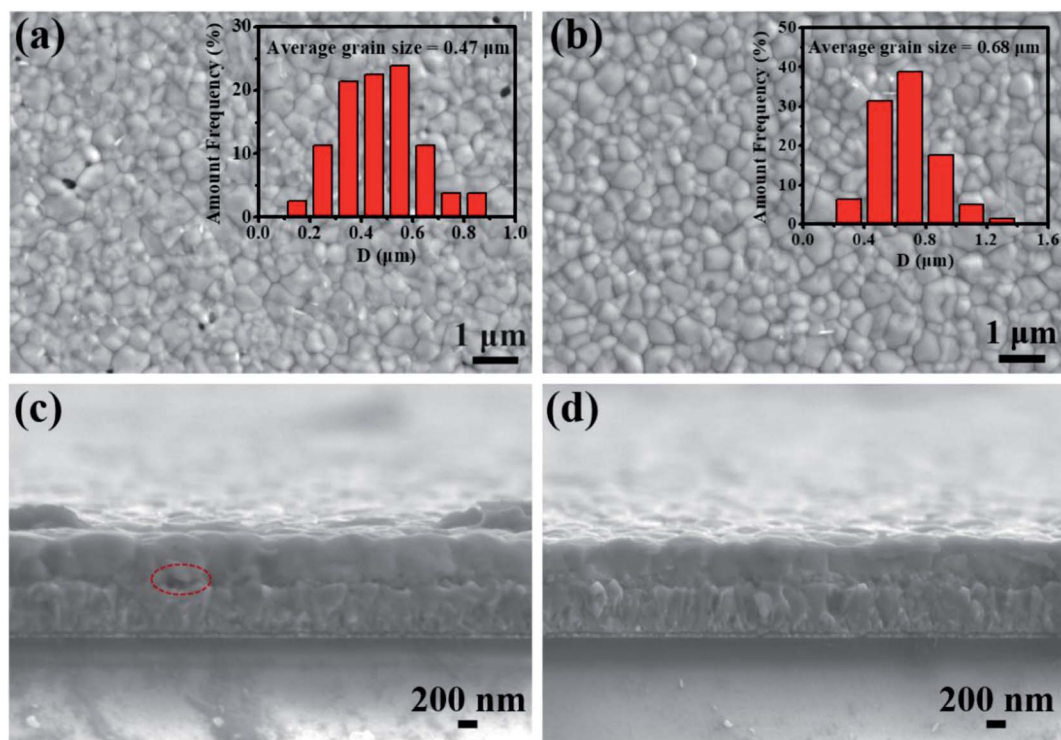

Fig. 3 FE-SEM images of (a) FTO/TiO$_2$/MAPbI$_3$ and (b) FTO/TiO$_2$/BaTiO$_3$:MAPbI$_3$. Cross section images of (c) FTO/TiO$_2$/MAPbI$_3$ and (d) FTO/TiO$_2$/BaTiO$_3$:MAPbI$_3$. The insets in (a) and (b) are the grain size distributions of the corresponding samples.
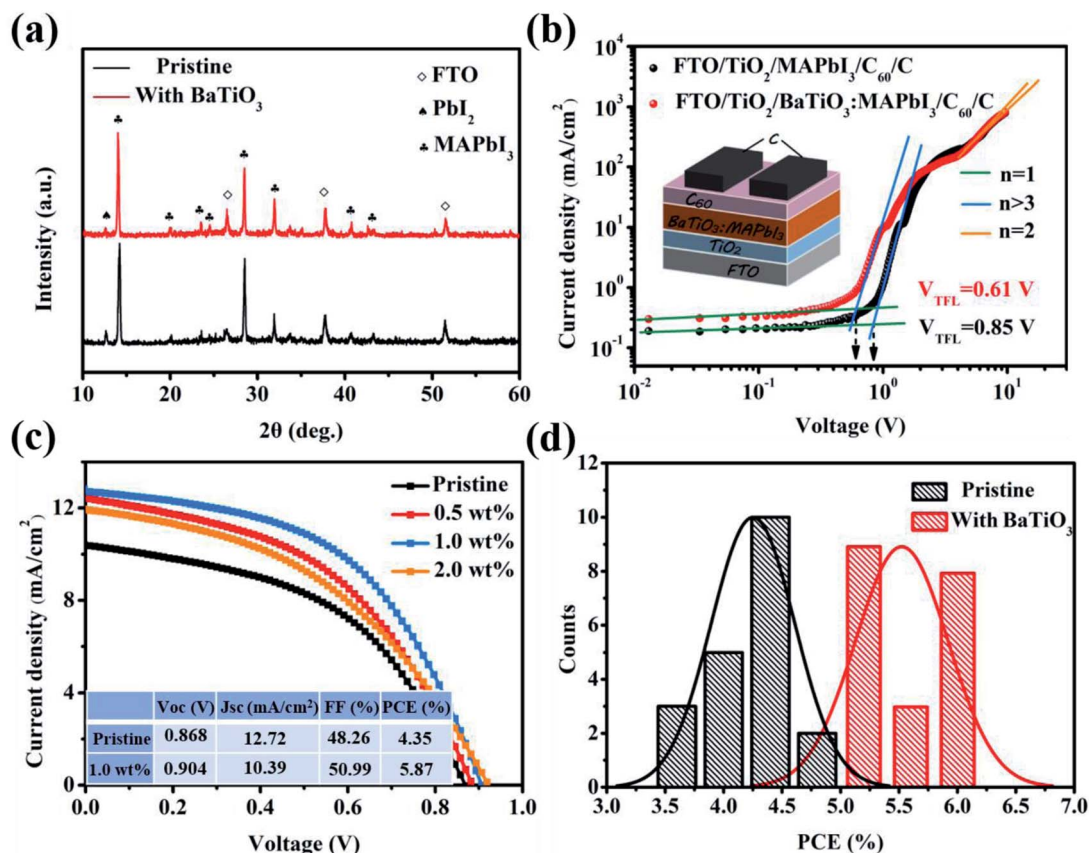
Fig. 4 (a) XRD patterns of MAPbI₃ and BaTiO₃:MAPbI₃. (b) SCLC tests based on the MAPbI₃ and BaTiO₃:MAPbI₃ single electronic devices. (c) $J-V$ characteristic curve of C-PSCs prepared with BaTiO₃ doped with MAPbI₃ at different concentrations. (d) Efficiency statistics of the MAPbI₃ and BaTiO₃:MAPbI₃-based C-PSCs.

$K\gamma/B\cos\theta$, the B value decreases (*i.e.*, the FWHM decreases), and the grain size D in the MAPbI₃ film will increase, which is consistent with the results of the FE-SEM image. In addition to the diffraction peaks of MAPbI₃ and FTO, the PbI₂ peak is also observed at 12.69°. When the content of PbI₂ is too high, it will affect the light absorption capacity of MAPbI₃, but the presence of a small amount of PbI₂ can passivate the perovskite grain boundaries, suppress the formation of defect states, and reduce the non-radiative recombination of the carriers.

To understand the effect of doping BaTiO₃ on the defection state density in the MAPbI₃ film, a single electron device with the structure FTO/TiO₂/(BaTiO₃):MAPbI₃/C60/C was prepared, and the transmission characteristics of the electronic transient process were studied by the SCLC testing method, as shown in Fig. 4(b).

$$V_{\text{TFL}} = eN_t d^2/2\varepsilon\varepsilon_0 \qquad (1)$$

where e is the unit charge, V_{TFL} is the trap-filled limit region voltage, N_t is the trap-state density, ε is the relative permittivity of MAPbI₃, ε_0 is the vacuum permittivity, and d is the thickness of the film. When the single-electron device is in the SCLC area, the $I-V$ curve in the dark state conforms to the Mott–Gurency formula:

$$J = 9\varepsilon\varepsilon_0\mu V^2/8L^2 \qquad (2)$$

where V is the applied bias voltage and μ is the electron mobility. We made the tangents at the two curves separately, and found that the V_{TFL} of the doped film is reduced from 0.85 V to 0.61 V. According to formula (1), the defection density of the original film is 1.21×10^{18} cm^{-3}. The defection density of the BaTiO₃ doped MAPbI₃ film reduced to 8.58×10^{17} cm^{-3}, indicating that the quality of the doped perovskite film is effectively improved, reducing the non-radiative recombination of the carriers, and endowing the carriers with longer diffusion. The length can pass through the MAPbI₃ film smoothly, which is also consistent with the results obtained by FE-SEM. Using formula (2) to calculate the dark current in the space-limited current region, the values of electron mobility μ of MAPbI₃ and BaTiO₃:MAPbI₃ single-electron devices are 5.43×10^{-5} cm^2 V^{-1} s^{-1} and 5.73×10^{-5} cm^2 V^{-1} s^{-1}, respectively.

Based on the addition of BaTiO₃ to improve the quality of the MAPbI₃ film, we fabricated C-PSCs with different concentrations of BaTiO₃ doped MAPbI₃ to study the effect of the doping concentration on the device performance. Fig. 4(c) shows the $J-V$ characteristic curves of C-PSCs prepared with different concentrations of BaTiO₃ under the condition of simulated sunlight with a light intensity of 100 mV cm^{-2}. As the

concentration increases in the range of 0–1.0 wt%, the performance of the device gradually improves. When the concentration further increases to 2.0 wt%, the performance of the device begins to decrease. Therefore, the performance of the device is optimal under the condition of the concentration of $BaTiO_3$ being 1.0 wt%. At this time, V_{OC} is 0.904 V, J_{SC} is 12.72 mA cm^{-2}, and FF and PCE are 50.99% and 5.87%, respectively. In order to ensure the reliability of the data, we prepared 40 samples and calculated the efficiency of C-PSCs before and after the addition of $BaTiO_3$. The PCE of the device is significantly improved and the discreteness is reduced after the addition of $BaTiO_3$, as shown in Fig. 4(d).

Fig. 5(a) shows the corresponding dark current curve. The dark current can characterize the internal leakage current and the defections in the device. It can be found that the dark current of the device is significantly reduced after doping with $BaTiO_3$. Combining with the FE-SEM and SCLC test results, it can be seen that the optimized device film is denser to avoid direct contact between the electron transport layer and the carbon electrode, thus effectively reducing the dark current of the device. At the same time, the defections of the doped film are reduced, which effectively inhibits the formation of the non-radiative recombination centers and reduces the non-radiative recombination. Fig. 5(b) shows the EQE curve of the C-PSCs

prepared based on the $MAPbI_3$ film and the $BaTiO_3$@$MAPbI_3$ composite film. The optimized device has an improved EQE value in the entire visible light wavelength range, which indicates that the doped $BaTiO_3$ can improve the collection efficiency of the photogenerated electrons. In order to further verify the positive influence of $BaTiO_3$ addition on the device, the actual output efficiency of the pristine sample and the optimized sample were tested. The corresponding voltages at the maximum output power point are 0.56 V and 0.65 V, respectively, and the test process is continued for 120 s under this bias voltage, as shown in Fig. 5(c). After illumination, the steady-state output current of the device rose rapidly and finally stabilized at 7.86 mA cm^{-2} and 8.68 mA cm^{-2}. Fig. 5(d) shows the impedance spectra of the two sets of devices, which are used to analyze the effect of doped $BaTiO_3$ nanoparticles on the carrier transport inside the device. The test bias voltage is 0.6 V and the test frequency is 1–1 MHZ. The curve is also fitted using Z-view software. R_S is reduced from 80.56 Ω to 47.78 Ω, and R_{rec} is increased from 3569 Ω to 5703 Ω, indicating the low interfacial contact resistance. The higher the carrier recombination resistance, the lower the degree of carrier recombination, which is conducive to carrier transmission and can reduce the probability of non-radiative recombination, leading to an increase in the V_{OC} and FF of the device.
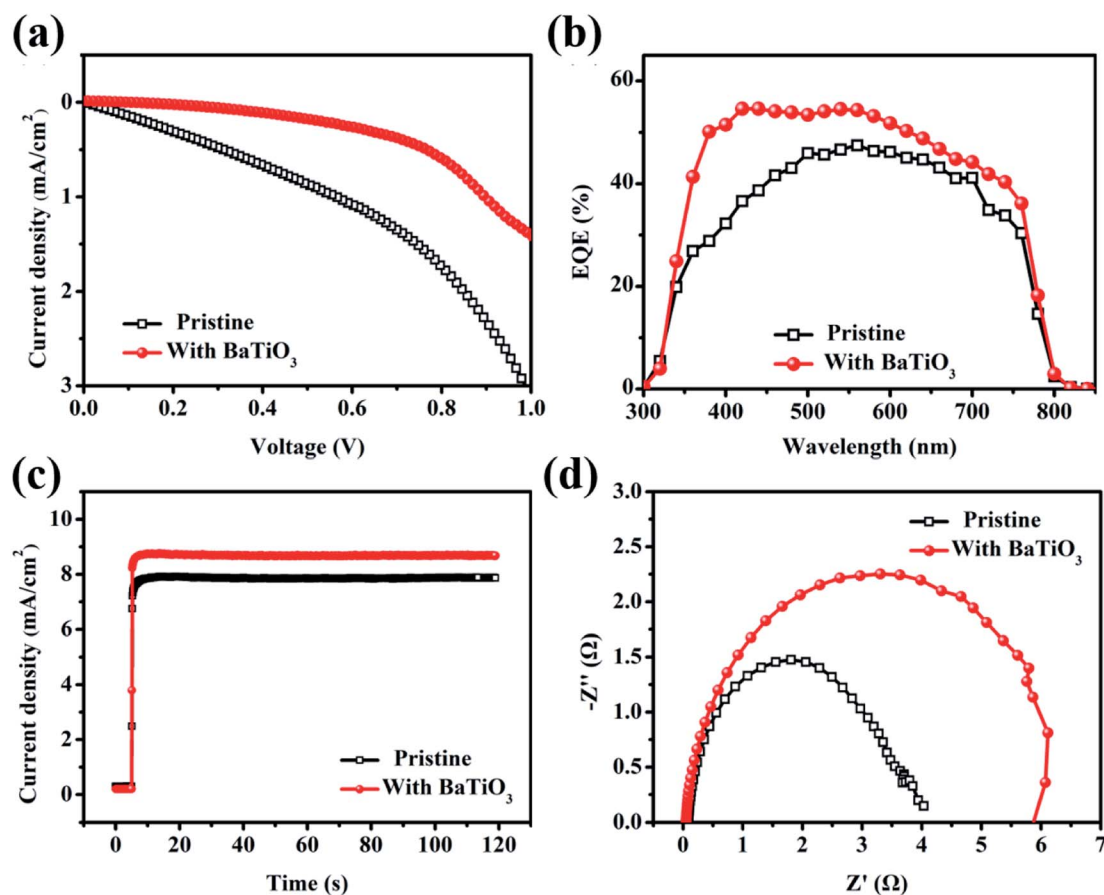

Fig. 5 (a) Dark current curve, (b) EQE curve, and (c) steady-state output current curve at the maximum power point. (d) Impedance diagram of the $MAPbI_3$ and $BaTiO_3$@$MAPbI_3$-based C-PSCs.

In order to maximize the action of the ferroelectric material, we prepared the BaTiO₃@MAPbI₃ composite film for polarization treatment, as shown in Fig. 6(a), and then assembled it into a cell with the structure to investigate the effect of the polarization voltage on the performance of PSCs. Fig. 7(a) shows the J–V curves of BaTiO₃@MAPbI₃ based on C-PSCs, and the corresponding photovoltaic performance parameters (listed in Table 1) under the conditions of polarization treatment with different polarization voltages. The performance of the cells with a polarization voltage of 2.0 V μm^{-1} is better than that of unpolarized cells, which further confirms the improvement of the polarization on the cell performance. When the applied voltage is 1.0 V μm^{-1}, the device performance is the best among these samples. The V_{OC} increases from 0.888 V to 1.005 V, J_{SC} increases from 13.47 mA cm^{-2} to 15.59 mA cm^{-2}, FF also increases from 47.10% to 56.40%, and the PCE of the device increases from 5.64% to 8.83%.

Subsequently, the Mott–Schottky test was used to characterize the changes in the built-in electric field of the cell. Firstly, the depletion layer approximate model was used to fit the curve, and the formula is as follows.

$$1/C^2 = (2/e\varepsilon\varepsilon_0 A^2 N_A)(V_{bi} - V) \tag{3}$$

$$N_A = 2/e\varepsilon\varepsilon_0 A^2 K \tag{4}$$

$$W = \sqrt{2\varepsilon\varepsilon_0(V_{bi} - V_{app})/qN_A} \tag{5}$$

where C is the capacitance at the interface between the light-absorbing layer and the ETL, N_A is the electron density, V_{bi} is the built-in electric field, and K is the Boltzmann constant. Fig. 7(b) is the Mott–Schottky curve of the BaTiO₃@MAPbI₃-based C-PSCs before and after polarization treatment. The intersection of the tangent line and the abscissa of the polarized C-PSCs is significantly shifted to the right compared to the pristine one. The obvious right shift indicates that V_{bi} significantly increases, and the slope of the tangent is significantly increased. The values of N_A, V_{bi}, and W of C-PSCs can be calculated according to Formulas (3)–(5). The detailed values can be found in Table 2. After polarization, the carrier concentration N_A decreases from 5.82×10^{15} cm^{-3} to 3.91×10^{15} cm^{-3}. The decrease in the carrier concentration, and the increase in the width of the depletion layer and the built-in electric field indicate that the residual polarization electric field generated by the iron polarization of the BaTiO₃ electric dipole promotes the bending of the interface energy band. This is conducive to the transmission of photogenerated carriers at the interface, thereby improving the performance of the cell.

The steady-state PL spectrogram, an important method, is used to investigate the carrier dynamics. The extraction rate of the carriers can be judged by comparing the degree of fluorescence quenching.[29] Fig. 7(c) shows the steady-state PL spectra of the BaTiO₃@MAPbI₃-based C-PSCs before and after polarization treatment. The fluorescence intensity of the device after polarization treatment is significantly reduced, indicating that the carriers can be transported faster from the perovskite film to the electron transport layer. This process can avoid non-radiative recombination caused by the recombination center. The corresponding voltage decay curve is shown in Fig. 7(d). After the polarization treatment, the voltage decay rate of the C-PSCs decreases to induce a longer internal carrier life of the device, which is consistent with the PL spectrum result. The residual polarized electric field formed by the dipole provides the transmission power for the carriers, which is the key element to the life extension.

According to the principle of semiconductor heterojunction, we assume that the parallel resistance (R_{sh}) is infinite, the leakage current of the device can be ignored,[30,31] and the I–V characteristic curve of a single heterojunction solar cell can be expressed as:[32]

$$-dV/dJ = [(AK_BT)/e](J_{SC} - J)^{-1} + R_S \tag{6}$$

where J is the current density through the external circuit load, R_S is the series resistance, A is the single-junction ideality factor, and T is the absolute temperature. We fitted the J–V curve of the MAPbI₃/BaTiO₃-based C-PSCs before and after polarization
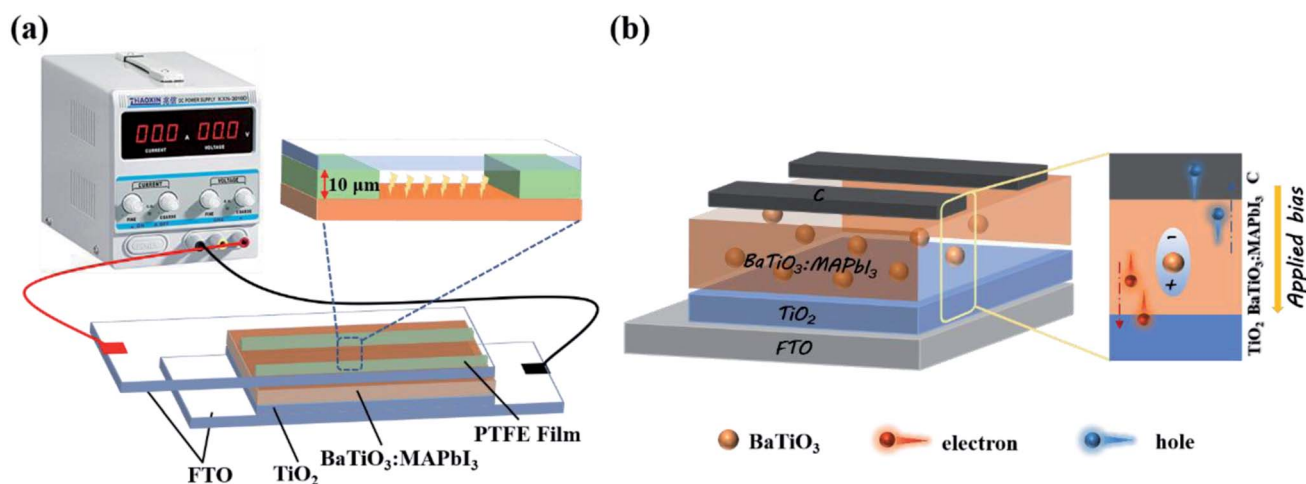

Fig. 6 (a) A diagram of the thin film polarization device. (b) Polarization schematic diagram of the C-PSCs.
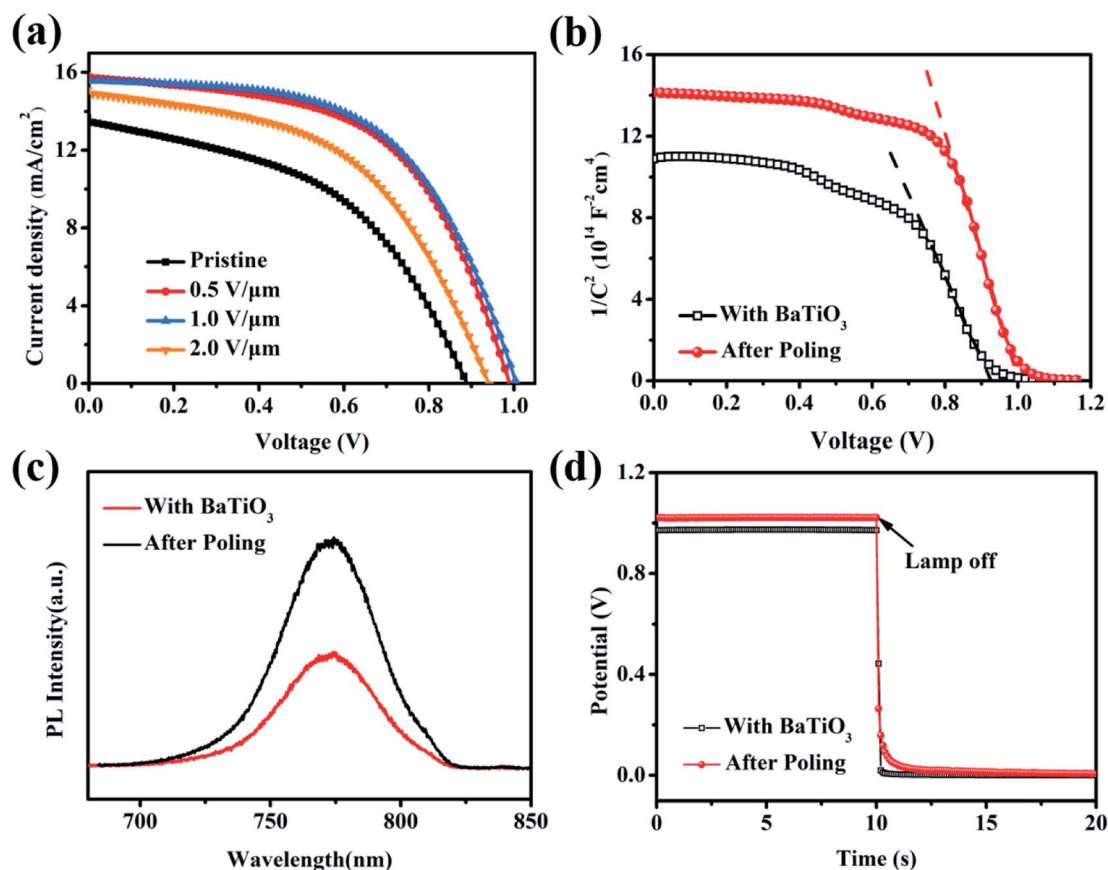
Fig. 7 (a) J–V characteristic curves of the BaTiO$_3$@MAPbI$_3$-based C-PSCs treated with different voltage polarization. (b) Mott–Schottky curves; (c) steady-state PL spectra; and (d) voltage attenuation curves of the BaTiO$_3$@MAPbI$_3$-based C-PSCs before and after polarization treatment.

Table 1 Photovoltaic performance parameters of the BaTiO$_3$@MAPbI$_3$-based C-PSCs polarized by different voltages

	V_{OC} (V)	J_{SC} (mA cm^{-2})	FF (%)	PCE (%)
Pristine	0.888	13.47	47.10	5.64
0.5 V μm^{-1}	0.989	15.72	55.66	8.65
1.0 V μm^{-1}	1.005	15.59	56.40	8.83
2.0 V μm^{-1}	0.940	14.92	50.57	7.09

Table 2 The N_A, V_{bi} and W values of the BaTiO$_3$@MAPbI$_3$-based C-PSCs before and after polarization treatment

	N_A (cm^{-3})	W (nm)	V_{bi} (V)
Pristine	0.888	13.47	47.10
0.5 V μm^{-1}	0.989	15.72	55.66
1.0 V μm^{-1}	1.005	15.59	56.40
2.0 V μm^{-1}	0.940	14.92	50.57

treatment to investigate the charge transfer characteristics inside the cell. As shown in Fig. 8(a), R_S decreases from 11.14 Ω cm^2 to 6.93 Ω cm^2 after polarization treatment, which is conducive for carrier transmission. Fig. 8(b) shows the relationship curve between the first derivative of the J–V curve and the voltage in the cell. The polarized cell shows better linear relationship near the open circuit voltage, indicating the reduced carrier collection barrier. Also, it is beneficial to improve the transmission efficiency of the carriers and reduce the probability of non-radiative recombination. Fig. 8(c) shows the corresponding EIS curve. The semicircle of the polarized cell in the low frequency region is extremely large. The EIS curve of the unpolarized C-PSCs is almost invisible in the whole picture, indicating that the non-radiative recombination of the carriers is greatly suppressed. It can also be verified from Fig. 8(d) that the R_{rec} value of unpolarized C-PSCs is only 5 kΩ, yet it rises sharply to about 50 kΩ after polarization treatment. It shows that the remnant polarization electric field generated by the electric dipole iron polarization provides power for carrier transfer and effectively inhibits the charge recombination of the device.

Finally, we further illustrate the principle of the performance caused by BaTiO$_3$ nanoparticles doped C-PSCs light-absorbing layer, as shown in Fig. 9. The specific explanation is divided into two points. Firstly, we doped BaTiO$_3$ nanoparticles with the C-PSCs light-absorbing layer, and the improvement in the cell performance is mainly caused by the increased quality of the light-absorbing layer film, leading to the improvement of the light absorption capacity. Furthermore, BaTiO$_3$ and MAPbI$_3$ are both regular octahedral
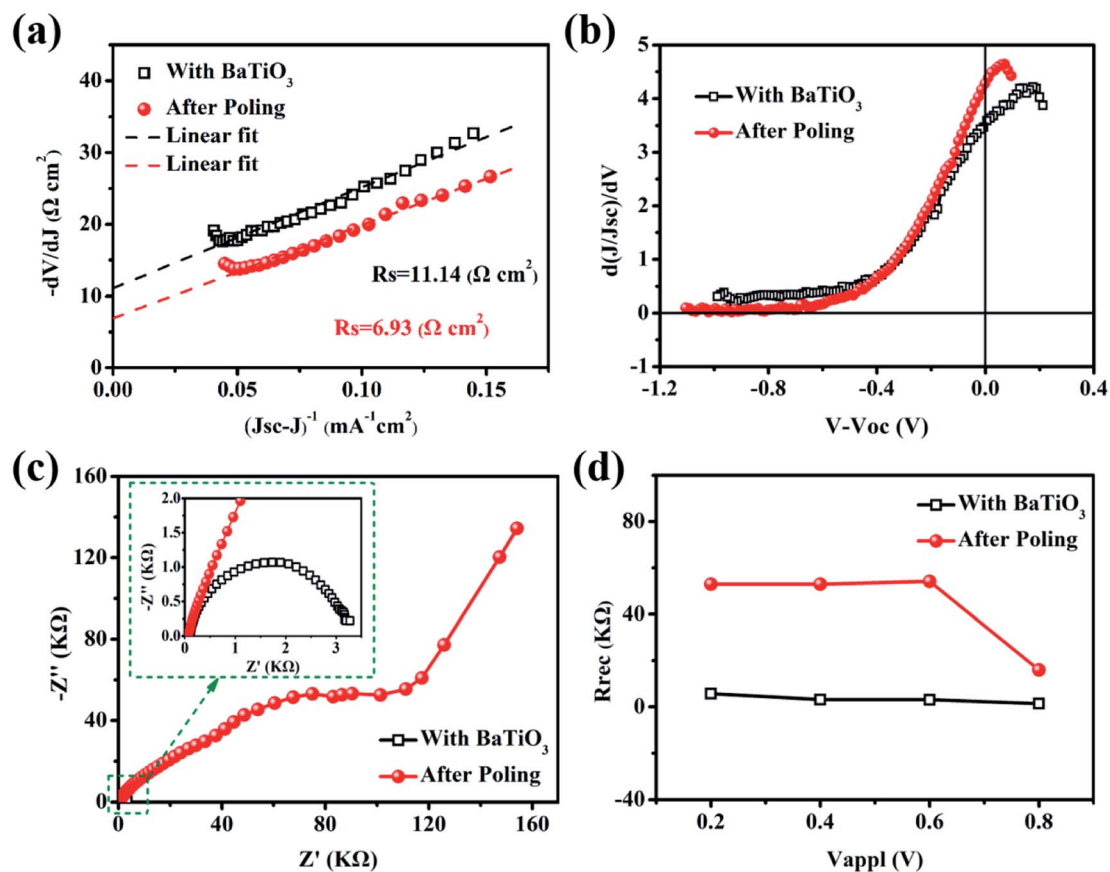
Fig. 8 (a) The relationship curve between $-dV/dJ$ and $(J_{SC} - J)^{-1}$. (b) Relationship curve between $\ln(J_{SC} - J)$ and $(V + R_S J)$. (c) EIS curve. (d) R_{rec} at different bias of the BaTiO$_3$@MAPbI$_3$-based C-PSCs before and after polarization treatment.
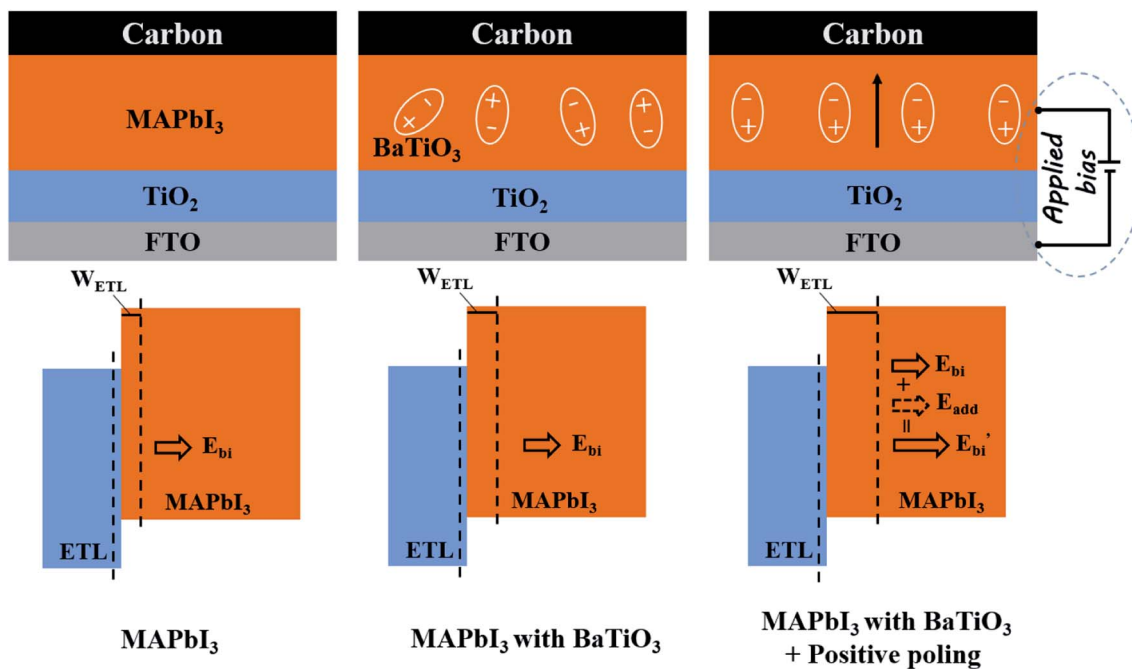

Fig. 9 Performance improvement schematic of the BaTiO$_3$@MAPbI$_3$-based C-PSCs.

structures. During the solvent volatilization and grain nucleation processes, $BaTiO_3$ can be used as the site for grain nucleation and growth, and can reduce the holes in the film. Also, the increased size of the crystal grains can improve the film coverage and uniformity, and the defects inside the film are reduced to promote carrier transmission. On this basis, when a positive external electric field is applied to polarize the ferroelectric dipole, the electric dipoles will be aligned under the action of the external electric field to form a polarized electric field, which is opposite to the direction of the external electric field. After the external electric field is removed, there can still be a residual polarization electric field E_{add} that is slightly smaller than the polarization electric field. E_{add} and E_{bi} have the same direction, and the built-in electric field inside the film increases to $E_{bi'}$. The width of the depletion layer W_{ETL} is changed at the same time so that the carrier transmission ability is further improved, and the non-radiative recombination is suppressed. It is mainly due to the effective regulation of the ferroelectric material on the carrier transport, resulting in the significantly improved performance of the cell.

4 Conclusions

In summary, $BaTiO_3$ was directly used as the additive in the perovskite precursor to prepare the $BaTiO_3@MAPbI_3$ composite film. The as-prepared perovskite film had better morphologies with the addition amount of 1.0 wt%. The crystallization performance of $MAPbI_3$ was improved with increased grain size, and the residual PbI_2 decreases to a certain degree, which effectively passivates the defects and reduces the defect state density. After the polarization treatment, the performance of the cell was significantly improved with the V_{OC} of the cell reaching 1 V, and the PCE was 8.83%. It is proved that the realization of high-performance C-PSCs comes from the residual polarization electric field induced by the ferroelectric material $BaTiO_3$. This can enhance the built-in electric field of the cell and increase the width of the depletion layer. Also, the increased driving force of carrier transport can promote the transport of the carriers and effectively suppress non-radiative recombination caused by the defects. The best device efficiency can reach 9.03% after optimization. This work mainly provides a possibility to design and develop optoelectronic devices with high-efficiency optoelectronic response behavior.

Conflicts of interest

There are no conflicts to declare.

Acknowledgements

References

1 A. Kojima, K. Teshima, Y. Shirai and T. Miyasaka, Organometal halide perovskites as visible-light sensitizers for photovoltaic cells, *J. Am. Chem. Soc.*, 2009, **131**(17), 6050–6051.

2 NREL, *Best Research-Cell Efficiency Chart*, https://www.nrel.gov/pv/cell-efficiency.html, accessed 17 March 2021.

3 L. Boudad, M. Taibi, A. Belayachib and M. Abd-lefdilb, Structural, morphological, dielectric and optical properties of double perovskites $RBaFeTiO_6$ (R = La, Eu), *RSC Adv.*, 2021, **11**, 40205–40215.

4 X. Zheng, Y. Deng, B. Chen, H. Wei, X. Xiao, Y. Fang, Y. Lin, Z. Yu, Y. Liu, Q. Wang and J. Huang, Dual functions of crystallization control and defect passivation enabled by sulfonic zwitterions for stable and efficient perovskite solar cells, *Adv. Mater.*, 2018, **30**(52), 1803428.

5 M. Kim, S. G. Motti, R. Sorrentino and A. Petrozza, Enhanced solar cell stability by hygroscopic polymer passivation of metal halide perovskite thin film, *Energy Environ. Sci.*, 2018, **11**(9), 2609–2619.

6 N. Shrivastav, J. Madan, R. Pandey and A. E. Shalan, Investigations aimed at producing 33% efficient perovskite-silicon tandem solar cells through device simulations, *RSC Adv.*, 2021, **11**, 37366–37374.

7 B. Chen, X. Zheng, M. Yang, Y. Zhou, S. Kundu, J. Shi, K. Zhu and S. Priya, Interface band structure engineering by ferroelectric polarization in perovskite solar cells, *Nano Energy*, 2015, **13**, 582–591.

8 C. Zhang, Z. Wang, M. Li, Z. Liu, J. Yang, Y. Yang, X. Gao and H. Ma, Electric-field assisted perovskite crystallization for high-performance solar cells, *J. Mater. Chem. A*, 2018, **6**, 1161–1170.

9 A. Stroppa, C. Quarti, F. D. Angelis and S. Picozzi, Ferroelectric Polarization of $CH_3NH_3PbI_3$: A Detailed Study Based on Density Functional Theory and Symmetry Mode Analysis, *J. Phys. Chem. Lett.*, 2015, **6**(12), 2223–2231.

10 F. Zheng, H. Takenaka, F. Wang, N. Z. Koocher and A. M. Rappe, First-principles calculation of the bulk photovoltaic effect in $CH_3NH_3PbI_3$ and $CH_3NH_3PbI_{3-x}Cl_x$, *J. Phys. Chem. Lett.*, 2015, **6**(1), 31–37.

11 T. Wang, B. Daiber, J. M. Frost, S. A. Mann, E. C. Garnett, A. Walsh and B. Ehrler, Indirect to direct bandgap transition in methylammonium lead halide perovskite, *Energy Environ. Sci.*, 2017, **10**(2), 509–515.

12 L. Leppert, S. E. Reyes-Lillo and J. B. Neaton, Electric field- and strain-induced Rashba effect in hybrid halide perovskites, *J. Phys. Chem. Lett.*, 2016, **7**(18), 3683–3689.

13 J. Beilsten-Edmands, G. E. Eperon, R. Johnson, R. D. Johnson, H. J. Snaith and P. G. Radaelli, Non-ferroelectric nature of the conductance hysteresis in $CH_3NH_3PbI_3$ perovskite-based photovoltaic devices, *Appl. Phys. Lett.*, 2015, **106**(17), 173502.

14 Z. Fan, J. Xiao, K. Sun, L. Chen, Y. Hu, J. Ouyang, K. P. Ong, K. Zeng and J. Wang, Ferroelectricity of $CH_3NH_3PbI_3$ Perovskite, *J. Phys. Chem. Lett.*, 2015, **6**(7), 1155–1161.

15 Y. Yuan, T. J. Reece, P. Sharma, S. Poddar, S. Ducharme, A. Gruverman, Y. Yang and J. Huang, Efficiency enhancement in organic solar cells with ferroelectric polymers, *Nat. Mater.*, 2011, **10**(4), 296–302.

16 Z. Xiao, Q. Dong, P. Sharma, Y. Yuan, B. Mao, W. Tian, A. Gruverman and J. Huang, Synthesis and Application of Ferroelectric P(VDF-TrFE) Nanoparticles in Organic Photovoltaic Devices for High Efficiency, *Adv. Energy Mater.*, 2013, **3**(12), 1581–1588.

17 H. A. Moghaddam, M. R. Mohammadi and S. M. S. Reyhani, Improved photon to current conversion in nanostructured TiO_2 dye-sensitized solar cells by incorporating cubic $BaTiO_3$ particles deleting incident, *Sol. Energy*, 2016, **132**, 1–14.

18 K. Feng, X. Liu, D. Si, X. Tang, A. Xing, M. Osada and P. Xiao, Ferroelectric $BaTiO_3$ dipole induced charge transfer enhancement in dye-sensitized solar cells, *J. Power Sources*, 2017, **350**, 35–40.

19 M. Wang, H. Feng, C. Qian, J. He, J. Feng, Y. Cao, K. Yang, Z. Deng, Z. Yang, X. Yao, J. Zhou, S. Liu and X. Zeng, $PbTiO_3$ as Electron-Selective Layer for High-Efficiency Perovskite Solar Cells: Enhanced Electron Extraction via Tunable Ferroelectric Polarization, *Adv. Funct. Mater.*, 2019, **29**(1), 1806427.

20 A. Pérez-Tomas, H. Xie, Z. Wang, H. Kim, I. Shirley, S. Turren-Cruz, A. Morales-Melgares, B. Saliba, D. Tanenbaum, M. Saliba, S. M. Zakeeruddin, M. Gratzel, A. Hagfeldt and M. Lira-Cantu, $PbZrTiO_3$ ferroelectric oxide as an electron extraction material for stable halide perovskite solar cells, *Sustainable Energy Fuels*, 2019, **3**, 382–389.

21 Y. Yang, Z. Liu, W. K. Ng, L. Zhang, H. Zhang, X. Meng, Y. Bai, S. Xiao, T. Zhang, C. Hu, K. Wong and S. Yang, An Ultrathin Ferroelectric Perovskite Oxide Layer for High-Performance Hole Transport Material Free Carbon Based Halide Perovskite Solar Cells, *Adv. Funct. Mater.*, 2019, **29**(1), 1806506.

22 X. Xu, L. Xiao, J. Zhao, B. Pan, J. Li, W. Liao, R. Xiong and G. Zou, Molecular Ferroelectrics-Driven High-Performance Perovskite Solar Cells, *Angew. Chem., Int. Ed.*, 2020, **59**(45), 19974–19982.

23 C. Zhang, Z. Wang, S. Yuan, R. Wang, M. Li, M. F. Jimoh, L. Liao and Y. Yang, Polarized Ferroelectric Polymers for High-Performance Perovskite Solar Cells, *Adv. Mater.*, 2019, **31**(30), 1902222.

24 H. Zarenezhad, M. Askari, M. Halali, N. Solati, T. Balkan and S. Kaya, Enhanced electron transport induced by a ferroelectric field in efficient halide perovskite solar cells, *Sol. Energy Mater. Sol. Cells*, 2020, **206**, 110318.

25 P. Zhu, Y. Chen and J. Shi, Piezocatalytic Tumor Therapy by Ultrasound-Triggered and $BaTiO_3$-Mediated Piezoelectricity, *Adv. Mater.*, 2020, **32**(29), 2001976.

26 H. Zhang, X. Wang, Z. Tian, C. Zhong and L. Li, Fabrication of Monodispersed 5-nm $BaTiO_3$ Nanocrystals with Narrow Size Distribution via One-Step Solvothermal Route, *J. Am. Ceram. Soc.*, 2011, **94**(10), 3220–3222.

27 Q. Jiang, Z. Chu, P. Wang, X. Yang, H. Liu, Y. Wang, Z. Yin, J. Wu, X. Zhang and J. You, Planar-structure perovskite solar cells with efficiency beyond 21%, *Adv. Mater.*, 2017, **29**(46), 1703852.

28 Z. Lu, S. Wang, H. Liu, F. Feng and W. Li, Improved efficiency of perovskite solar cells by the interfacial modification of the active layer, *Nanomaterials*, 2019, **9**(2), 204.

29 A. Mei, Y. Sheng, Y. Ming, Y. Hu, Y. Rong, W. Zhang, S. Luo, G. Na, C. Tian, X. Hou, Y. Xiong, Z. Zhang, S. Liu, S. Uchida, T. Kim, Y. Yuan, L. Zhang, Y. Zhou and H. Han, Stabilizing Perovskite Solar Cells to IEC61215: 2016 Standards with over 9000-h Operational Tracking, *Joule*, 2020, **4**(12), 2646–2660.

30 C. Liu, Z. Qiu, W. Meng, J. Chen, J. Qi, C. Dong and M. Wang, Effects of interfacial characteristics on photovoltaic performance in $CH_3NH_3PbBr_3$-based bulk perovskite solar cells with core/shell nanoarray as electron transporter, *Nano Energy*, 2015, **12**(1), 59–68.

31 Z. Jiang, Z. Xiao, Z. Tao, X. Zhang and S. Lin, A significant enhancement of bulk charge separation in photoelectrocatalysis by ferroelectric polarization induced in $CdS/BaTiO_3$ nanowires, *RSC Adv.*, 2021, **11**, 26534–26545.

32 S. S. Hegedus and W. N. Shafarman, Thin-film solar cells: device measurements and analysis, *Prog. Photovoltaics*, 2004, **12**(2–3), 155–176.